다중 조화 제어 및 유체-구조 연계 해석을 통한 고속 복합형 동축 반전 회전익기의 능동적 진동 저감 연구

Multicyclic Vibration Control of Lift-Offset Coaxial Rotorcraft using CFD/CA Coupling

초록

본 연구에서는 고속 전진 비행 시 다중 조화 개별 블레이드 제어(IBC) 기법을 적용하여 동축 반전 로터의 능동 진동 저감을 수행했다. 고충실도 공력기계학적 해석을 위해 전산유체해석(CFD)과 회전익 통합 해석 코드(CA)의 상호 연성 연계 연구를 했으며, 이를 통해 도출된 진동 하중 예측 결과를 비행 시험 데이터와 비교하여 그 타당성을 검증했다. 개회로 제어를 통해 진동 저감에 효과적인 IBC 작동 주파수를 식별하고, 폐회로 제어를 통해 최적 다중 조화 제어 입력을 산출했다. 결정된 최적 제어 시나리오는 진동 지수를 기준 대비 최대 84.7% 감소시키는 것으로 나타났으며, CFD/CA 연계 기반의 다중 조화 IBC 제어가 리프트 옵셋 로터 시스템에 대해 효과적인 진동 저감 방안이 될 수 있음을 확인했다.

Key Words : Lift-offset rotorcraft, CFD/CA coupling, Vibration reduction, Multicyclic control

Introduction

Recently, the development of high-performance rotorcrafts with significantly increased flight speeds and high-performance rotorcrafts with significantly increased flight speeds and high maneuverability has attracted special attention globally[1~3]. As the forward speed increases, the edgewise rotor encounters significant variations in blade incoming air velocities between the advancing and the retreating sides. Consequently, the aerodynamic environments over the rotor disk become increasingly complex leading to high vibration and excessive loads of the vehicle. Various types of rotorcrafts including tilting concepts and compound configurations have been devised and tested to overcome the limitations of conventional helicopters. The XH-59A is a pioneering aircraft that adopts the Advancing Blade Concept (ABC) scheme, enabling the roll moment control using two counter-rotating rotors through the lift-offset (L.O.) mechanism without interfering with the aerodynamic deficiencies in the retreating sides. Notably, the XH-59A reached a maximum forward speed of 160 knots in helicopter mode and 240 knots in level cruise mode with auxiliary propulsion[4,5]. Despite the accomplishments, the test program was terminated due to severe vibrations and high fuel consumptions encountered during the flight.

A number of studies have been conducted to identify the sources of high vibrations of L.O. coaxial helicopters using comprehensive aeromechanics (CA) analysis with rotors in isolation[6,7]. Previous studies[8~12] incorporated a finite element (FE) fuselage model to examine the rotor-body coupled vibration and its active suppression for L.O. coaxial compound helicopters. Blackwell et al.[8] employed a three-dimensional (3D) FE model with an active vibration control system (AVCS) to reduce cockpit vibrations in high-speed flight. Lee et al.[9] combined individual blade control (IBC) and AVCS schemes to suppress the overall vibration of the XH-59A vehicle. These studies[8,9] adopted a one-way rotor-body coupled approach, neglecting the motion of the fuselage in vibratory hub loads predictions. In former studies[10~12], the vibration reduction of an XH-59A rotorcraft using an interactive rotor-body coupling was performed using IBC schemes. A parametric sweep study in terms of actuation amplitudes and phase angles of IBC inputs was conducted, resulting in significantly reduced vibrations in the cockpit (below 0.05g)[10]. Hong et al.[12] explored vibration reduction of XH-59A rotorcraft using a multicyclic controller approach. The optimal control inputs were obtained by either open- or closed-loop control using an identified offline rotor system, which accomplished substantially reduced vibration levels at the pilot seat. These studies were conducted using low fidelity CA analysis methodologies with

various levels of inflow models. While these studies have demonstrated an effective means of vibration suppression with reasonable computational costs, they often rely on simplified aerodynamic models with the deficiency of describing the detailed flow physics of the rotor.

In addition to the low-fidelity comprehensive analyses, recent high-fidelity CFD studies have also been conducted to investigate the unsteady aerodynamic characteristics of coaxial rotor in forward flight. Hayami et al.[13] performed CFD simulations at high advance ratios, demonstrating that thrust fluctuations induced by blade crossing events of coaxial rotors become increasingly significant and cannot be accurately captured by low-order aerodynamic models. Yuan et al.[14] studied rotor-wake interactions of a coaxial rotor using a high-order numerical scheme, revealing strong inter-rotor BVI (Blade-Vortex Interaction) effects, particularly affecting the lower rotor. While these full-CFD approaches have contributed to advance the fundamental understanding of complex flow phenomena for L.O. coaxial rotor system, they inherently lack the capability to consider the instantaneous elastic deformation of the blades and their interaction with the vortex system, essentially affecting the rotorcraft vibration. To overcome these limitations and enhance the prediction capabilities on the vibration sources and their responses, the first principle-based high-fidelity method which combines the CFD and CA codes is necessary to be explored.

In the rotorcraft aeroelastic analysis, the concept of CFD/CA coupling originates from the work of Tung et al.[15], who introduced a loosely coupling (LC) algorithm wherein CFD and CA solvers exchange the other's data on a periodic basis. This innovative scheme has evolved to counter the unresolved aeroelastic challenges highlighted in earlier works[16,17], particularly associated with the UH-60A airloads program. Among others, the CFD/CA LC algorithm has been successfully adopted to various rotors as UH-60A[18,19], 7A[20,21], HART I[22], and HART II[23,24]. These and numerous other efforts have contributed to significant advances in the prediction capability and improved understanding of many rotorcraft aeromechanics phenomena[18~24]. However, most of the studies conducted so far have been limited to the conventional single-rotor configuration helicopters. One of a few exceptions is the work by Jia and Lee[25], who adopted a loosely coupled CFD/CA methodology to L.O. coaxial rotors for enhanced aerodynamic and aeroacoustic prediction of the rotor. This high-fidelity simulation exhibited success in capturing unsteady phenomena such as BVI and blade crossing events of the counter-rotating coaxial rotors. Min et al.[26] developed a full-vehicle analysis model for the SB>1 Defiant® compound rotorcraft and validated its performance prediction against flight test data using CFD/CA coupling. The results demonstrated high accuracy in predicting rotorcraft performance, hub drag, and trim sensitivity of the vehicle in high-speed flight. However, these analyses focused on aerodynamic aspects and no other attempts have been made to examine the structural dynamics or vibrational features of L.O. coaxial rotors which should be of prime concern to this class of the rotorcraft, especially in high-speed flight regime.

In this work, a CFD/CA coupling approach is employed to perform the optimal vibration reduction of a L.O. coaxial rotor using the multicyclic control scheme. To this end, rotorcraft CA code CAMRAD II[27] and 3D compressible Reynolds-Averaged Navier Stokes (RANS) flow solver KFLOW[28] are combined in a LC method[29]. The present study aims at: assessing the accuracy of the CFD/CA coupled analysis in reference to flight test data in high-speed flights; applying multicyclic harmonic inputs to identify optimal actuation strategies for rotor vibration reduction; and evaluating the vibration reduction gains obtained by the CFD/CA LC analysis with respect to CA with rolled-up free wake model. The parametric sweep results are also compared with those of the closed-loop control to confirm and verify the optimum vibration reduction gains of the rotor. Based on the literature survey results, the present work is believed to be the first attempt to explore the CFD/CA LC approach to investigate the rotor hub vibration and apply optimal control for active vibration suppression of L.O. coaxial rotor.

CFD/CA coupled analysis

CA analysis model

The rotorcraft comprehensive analysis code CAMRAD II[26] is employed to trim and analyze the L.O. coaxial rotor system. CAMRAD II is characterized by multibody dynamics, nonlinear FE formulation, and various levels of rotorcraft aerodynamic models. Figure 1 shows the overall configuration of the L.O. coaxial rotorcraft XH-59A, including the 3-bladed counter rotating rotors with auxiliary propulsion units. Figure 2 illustrates the present aerodynamic and structural models of CAMRAD II for XH-59A rotor system[12]. Structurally, each blade is discretized into 13 beam FEs, with 15 degrees of freedom (DOFs) per element which includes three axial, two flap, two lag, and two torsional motions. A pitch link model with a spring constant of 135,582 N/m is used to tune the pitch control system of the rotor[5]. The blade stiffnesses are modified to closely match with the measured nonrotating frequencies of the rotor while adjusting the flap- and lag-bending stiffnesses to about 80% and 85% of the baseline values, respectively. The aerodynamic model consists of 18 panels (see Fig. 1), using the ONERA-EDLIN unsteady airfoil theory in conjunction with C81 airfoil table. A rolled-up free-wake model with a dual-peak feature is used to represent the inflow distribution around the rotor. The dual-peak model accounts for the negative lift typically present near the advancing blade tip in high-speed flights. The aerodynamic interaction effects between the upper and lower rotors are also taken into consideration by a general free-wake geometry framework[30].

Fig. 1. XH-59A lift-offset rotorcraft

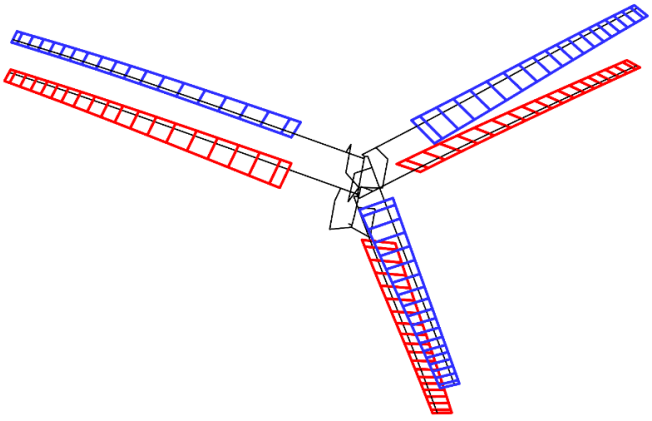

Fig. 2. CA analysis model of XH-59A rotor

The rotor trim analysis is conducted using six independent pitch control inputs and six corresponding trim targets set for level cruise conditions of the L.O. coaxial rotor system. The trim variables include the mean and differential collective angles for both rotors as well as the longitudinal and lateral cyclic pitch angles for each rotor. The goal of the trim is to achieve a moment balance between the upper and lower rotors by adjusting the pitch controls so that the mean and differential moments (roll and pitch) remain in equilibrium while satisfying the target L.O. value. To this purpose, the total rotor lift is matched to the gross weight of the vehicle, with the torque equilibrium between the rotors is enforced. The L.O. is defined as a function of the rotor-generated lift L, rotor radius R, and differential roll moment ΔM_X as:

$$\text{L.O.} = \frac{\Delta M_X}{L \cdot R} \tag{1}$$

An isolated rotor model is used to simplify the analysis. The rotor rotational speed is maintained at 98% of the nominal RPM, considering the flight test records[4]. To quantify the hub vibration level of the rotorcraft, a vibration index (VI) is introduced, defined in accordance with the criteria specified in ADS-27A-SP[31]:

$$\mathrm{VI}=\left\{\beta_1\frac{\sqrt{\left(0.5F_X\right)^2+\left(0.67F_Y\right)^2+\left(F_Z\right)^2}}{W_0}+\beta_2\frac{\sqrt{\left(M_X\right)^2+\left(M_Y\right)^2}}{W_0R}\right\} \quad (2)$$

where F_X, F_Y, and F_Z are the hub forces in the longitudinal, lateral, and vertical directions, respectively and M_X and M_Y are the rolling and pitching moments, respectively. In addition, W_0 is the vehicle weight, and β_i ($0 \le \beta_i \le 1$, $i = 1, 2$) are the weighting factors, respectively. Unless otherwise stated, only 3P components of vibration indices are considered. For the performance measure, the effective lift-to-drag ratio (L/D_e) of the rotor is used to evaluate the efficiency of the rotor in forward flight as given by:

$$L/D_e = L\cdot V/(P_i+P_0) \quad (3)$$

where V is the forward speed, and P_i and P_0 are the induced and profile power of the rotor, respectively.

CFD model

The CFD analysis is conducted using KFLOW[28], a 3D compressible RANS solver optimized for parallel computation within multiblock structured domains. The KFLOW conducts high-fidelity simulations of unsteady rotor flows by employing a Chimera overset grid scheme, enabling accurate modeling of moving bodies such as rotating blades. The temporal accuracy is achieved through a second-order dual-time stepping algorithm combined with a diagonalized alternating directional implicit method. For the spatial discretization, Roe's FDS (Flux Difference Splitting) method is used for inviscid flux computations as well as the fifth-order WENO (Weighted Essentially Non-Oscillatory) scheme to preserve the solution quality near the region with sharp gradients. The viscous terms are treated using a central-difference scheme, and the fully turbulent flow is modeled using the k-ω Wilcox-Durbin model. At the boundaries, a characteristic boundary condition based on the Riemann invariants is applied at the far-field, with the no-slip condition enforced at solid surfaces. The computational grid system is composed of Chimera moving grids for the blades and Cartesian off-body background meshes. Near the blade surface, a C-H type topology is adopted to form the grids (Fig. 3(a)). The full grid system constructed for the isolated coaxial XH-59A rotor is shown in Fig. 3(b). Each blade is discretized into 68×119×281 grid points in the normal, spanwise, and chordwise directions, respectively, totaling about 2.21M (million) cells per the blade. The background mesh, defined in the vertical, lateral, and longitudinal axes, contains 125×377×377 grid points. A grid spacing of 0.1c (chord length) is used in the off-body domain. The complete mesh system which includes the near-body blade grids and the Cartesian off-body grids, overall resulting in approximately 30.8M cells for the isolated coaxial rotor configuration.

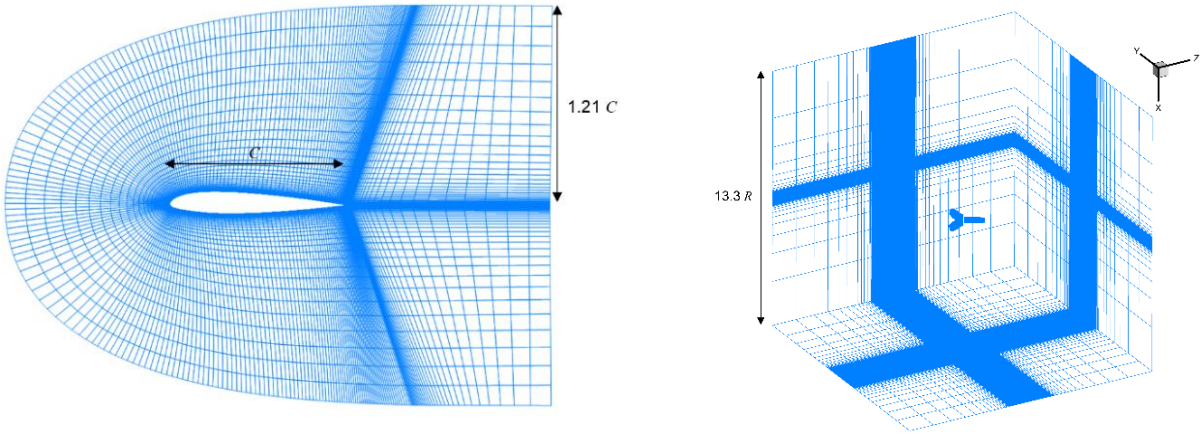

(a) Blade grid system (b) Overall grid system

Fig. 3. Computational grid system for isolated XH-59A rotor

CFD/CA LC analysis

An LC algorithm is employed to systematically integrate the CA and CFD solvers. The coupling is performed on a per-revolution (P) basis, wherein the computed blade deformation and trim control angles from the CA analysis are transferred to the CFD solver to evaluate the unsteady aerodynamic loads based on the changed motions. The LC iteration begins with a CA trim analysis using a lifting-line aerodynamic model. The trim solution is found within the CA framework using six independent pitch control inputs and six corresponding trim targets, which include the mean and differential collective, and longitudinal and lateral cyclic angles for each rotor. The trim is set to achieve the desired moment balance between the upper and lower rotors while satisfying the specified L.O. value. In addition, the rotor lift is matched to the vehicle weight with the torque balance is maintained. The resulting pitch control angles and blade motions are passed to the CFD solver, which computes the aerodynamic forces and moments over the rotor revolution. The difference in airloads (called delta airloads) between CFD and CA predictions is then fed back to the CA code to update the blade motions and trim controls. The exchange of information with each other continues until a convergence is met in pitch control settings, airloads, delta airloads, and blade motions of the rotor. Typically, the initial CFD analysis runs three rotor revolutions to achieve a stable flow condition, while subsequent iterations are proceeded one rotor revolution using a restart option from the previous step. This allows an efficient and accurate evaluation of aeroelastic responses of the coaxial rotor system in steady level flight condition.

Multicyclic vibration control

Figure 4 shows the schematic of a multicyclic vibration control system described in the frequency domain, aiming to reduce the vibration of a rotor system. The rotor experiences periodic loads having a variety of frequency contents in the rotating frame and nN_b P in the non-rotating frame, respectively, during the flight. The fixed-frame loads nN_b P represent the blade passage frequencies (BPF) where n is an integer and Nb the number of blades, respectively. The control inputs required to suppress the vibratory harmonics will also be periodic, which are generated in the control command system. A time-domain signal of the control command should be generated to activate the actuators while considering the dynamics of the rotorcraft.

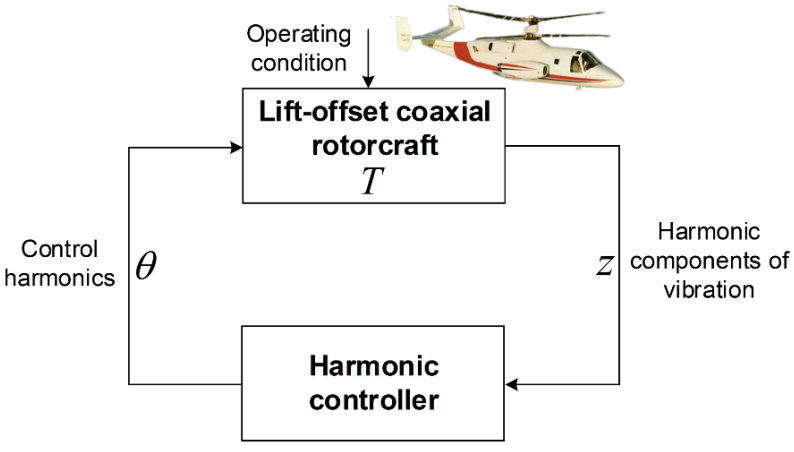

Fig. 4. Flow diagram of multicyclic control of L.O. rotorcraft

Model identification

Two different modeling approaches can be employed to represent the multicyclic control system: the local model or the global model. The local model is linear with respect to the current control input, whereas the global model assumes linearity across the full control range. In this study, the global model

is adopted to represent the L.O. coaxial rotor, as illustrated in Fig. 3. The global model can be written as:

$$z_k = z_0 + T\theta_k \tag{4}$$

The vibratory response at the k–th step is obtained by the initial condition of the L.O. rotorcraft using the transfer function with the multicyclic control inputs. The rotorcraft is assumed to behave in a linear and quasi–static frequency domain. A detailed formulation using the simulated transfer function $\hat{T}$ for the present L.O. rotorcraft can be found in the former study[12].

Optimal control solution

The control algorithm is established using the minimization of the performance function. The performance function is defined in quadratic form as:

$$J = z_k^T W_z z_k + \theta_k^T W_\theta \theta_k + \Delta\theta_k^T W_{\Delta\theta} \Delta\theta_k \tag{5}$$

where $\Delta\theta_k = \theta_k - \theta_{k-1}$ is at the k–th step, W_z, W_θ, and $W_{\Delta\theta}$ are the weighting matrices for the responses, control inputs, and control rates, respectively. The weighting matrices are typically diagonal with all entries set to the same value, implying equal importance to all harmonic contents. Then the performance J is a weighted sum of the mean squares of the vibration and control. The optimal control input to alleviate the helicopter vibration is obtained by substituting z_k into the performance function, and solving for θ_k that minimize J. Setting $\partial J/\partial\theta_k = 0$ with the condition of $\partial z_k/\partial\theta_k = \mathrm{T}$ results in:

$$T^T W_z z_k + W_\theta \theta_k + W_{\Delta\theta} \Delta\theta_k = 0 \tag{6}$$

Substituting Eq. (4) into Eq. (6) gives,

$$\theta_k = C z_0 + C_{\Delta\theta} \theta_{k-1} \tag{7}$$

where the gain matrices are defined as: $C = -DT^T W_z$ and $C_{\Delta\theta} = DW_{\Delta\theta}$ with $D = (T^T W_z T + W_\theta + W_{\Delta\theta})^{-1}$. The general solutions that can be applied to the local and global models are given as[32]:

$$\theta_k = C z_{k-1} + (C_{\Delta\theta} - CT)\theta_{k-1} \tag{8}$$

Open–loop control

The optimal solution for the global model of Eq. (7) defines an open–loop control system determined from the uncontrolled response z_0 and the previous control input θ_{k-1}. There will be no feedback of the measured response. With the control rate $W_{\Delta\theta} = 0$, the open–loop control solution reduces to:

$$\theta_{\mathrm{opt}} = C z_0 \tag{9}$$

The control input is independent of the previous control input and determined using the uncontrolled response z_0. The schematic of the present open–loop multicyclic control system is shown in Fig. 5. The optimal multicyclic input identified in the open–loop will then be used as the multicyclic closed–loop control actuation of the aircraft model as described in the following section.

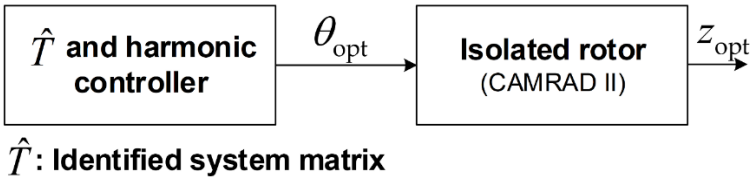

Fig. 5. Open–loop multicyclic control procedure

Closed-loop control using CFD/CA LC analysis

The optimal control solutions of the global and local models define a closed-loop control obtained by the feedback of the measured response z_{k-1}. For the global model with no estimation error (i.e., $\hat{T} = T$), the control command converges to the optimal solution in one cycle. When a small amount of measurement noise is existed, Eq. (5) will act as a closed-loop controller. A practical method of implementing a closed-loop controller is to use a gradient descent approach. The gradient descent is an optimization algorithm used to minimize the performance function by iteratively moving in the direction of the steepest descent as dictated by the negative of the gradient. For the performance function defined in Eq. (5), the steepest descent of the performance function is expressed as:

$$\theta_{k+1} = \theta_k - \frac{\alpha}{2}\frac{\partial J}{\partial \theta_k} \tag{10}$$

where α is the step-size. The instantaneous gradient is derived by partially differentiating the performance function (Eq. 5) with respect to the control input θ_k as:

$$\begin{aligned}\frac{\partial J}{\partial \theta_k} &= 2\left(\frac{\partial z_k}{\partial \theta_k}\right)^T W_k z_k + 2W_\theta \theta_k + 2W_{\Delta\theta}\theta_k \\ &= 2(T^T W_z z_k + W_\theta \theta_k + W_{\Delta\theta}\Delta\theta_k)\end{aligned} \tag{11}$$

Then, the control command update is described in the following form:

$$\theta_{k+1} = \theta_k - \alpha(T^T W_z z_k + W_\theta \theta_k + W_{\Delta\theta}\Delta\theta_k) \tag{12}$$

Figure 6 illustrates the flow diagram of the closed loop multicyclic control through using the CFD/CA LC algorithm. The process begins with a CFD/CA LC analysis for a converged delta airloads. Next, an open-loop controller is engaged to identify the dominant harmonic frequency contents that can effectively reduce the hub vibration. This is materialized using the initial vibratory responses and the converged delta airloads obtained using the CFD/CA LC trim analysis. The identified optimal frequency components are then employed in the closed-loop controller, where the IBC control input at the k-th iteration (denoted by θ_k) is updated using a gradient descent algorithm (Eq. 10). A new CA trim analysis is subsequently conducted using the updated control inputs θ_k and the converged delta airloads. The updated rotor trim angles, control inputs and blade motions from the CA analysis are passed to the CFD solver to compute the new delta airloads at the k-th step. These are then fed back to the CA analysis to update the vibratory response. This loop continues until the rotor hub vibration converges within the desired tolerance while yielding the optimal control input θ_{opt}.

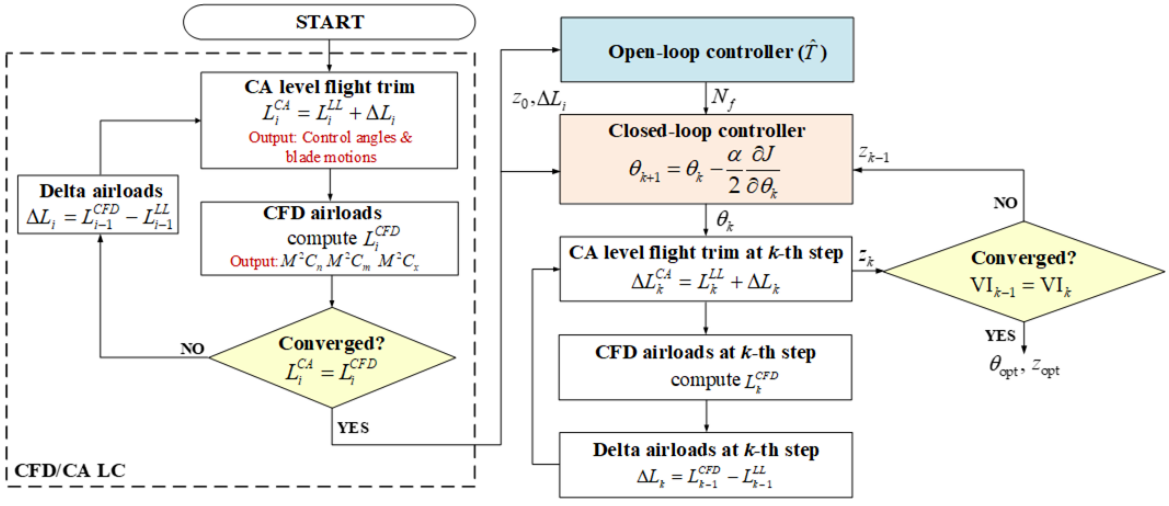

Fig. 6. Closed-loop multicyclic control procedure using CFD/CA LC analysis

Multicyclic IBC controller

The present study explores the IBC actuation installed at the pitch link, to actively suppress the vibration of both the upper and lower rotors. The blade pitch motion including the IBC actuation is defined as:

$$\theta_P(\psi) = \theta_0 + \theta_{1c}\cos\psi + \theta_{1s}\sin\psi + A_n\cos(n\psi - \Phi_n) \tag{13}$$

where θ_P is the blade instantaneous pitch angle at the specified azimuthal angle ψ, and $\theta_0, \theta_{1c}, \theta_{1s}$ are the collective pitch, lateral cyclic, and longitudinal cyclic angles, respectively. In addition, n is the actuation frequency of the IBC harmonic pitch input, A_n is the amplitude, and Φ_n is the phase angle, respectively. To compose the response matrix Z (response vector of z with K measurement set), the response vector z is defined as follows:

$$z = [F_{Xc}F_{Yc}F_{Zc}M_{Xc}M_{Yc}M_{Zc}F_{Xs}F_{Ys}F_{Zs}M_{Xs}M_{Ys}M_{Zs}]^T \tag{14}$$

where only the first BPF content of 3P has been kept, as stated previously. The multicyclic control vector θ defined in terms of 2P, 3P, and 4P harmonics of the rotor is given by:

$$\theta = [\cos 2\mathrm{P}\ \sin 2\mathrm{P}\ \cos 3\mathrm{P}\ \sin 3\mathrm{P}\ \cos 4\mathrm{P}\ \sin 4\mathrm{P}]^T \tag{15}$$

where each entity indicates the cosine and sine amplitudes of the respective frequency inputs. Each single harmonic actuation scenario is processed using the parametric sweep study to compose the basic response vector of the z. The IBC actuation inputs involved in the parametric sweep are the pitch amplitudes, frequency contents, and phase angles, respectively. The amplitudes range from 0 to 2.0 deg. (with an increment of 0.5 deg.), with the changes in phase angles at every 30 deg. A total of 144 IBC actuation scenarios are computed to develop the response vector Z of the rotorcraft which consists of a 12 by 144 matrix. For the multiple harmonic actuation case, the last term of the IBC pitch input in Eq. (13) is modified as:

$$\theta_{nc}(\psi) = \sum_{n \in N_f} A_n\cos(n\psi - \Phi_n) \tag{16}$$

where θ_{nc} denotes the multicyclic harmonic pitch input which is comprised of different frequency contents N_f, dependent upon the actuation scenarios.

Results and discussion

The XH-59A in cruise flights is analyzed using the CFD/CA LC analysis. The flight conditions of either 150 knots or 200 knots are considered to validate the CFD/CA LC predictions and confirm the correct treatment of the trim methodology adopted in the analysis. Subsequently, the 200 knots case (μ = 0.53) is analyzed to evaluate the effectiveness of an optimal vibration reduction of the coaxial rotor with the multicyclic IBC controller.

Trim convergence

Figure 7 presents the iteration histories of CFD/CA coupling, specifically for the CA trim control angles and the corresponding CFD trim values. As can be seen, the trim variables exhibit clear convergence trends as the coupling iteration is marched. Figure 7(a) presents the behavior of the trim control angles obtained by the CA analysis at each iteration step where the solid lines represent the upper rotor and the dotted lines denote the lower rotor. The converged trim control angles are subsequently post-processed and fed to the CFD solver to compute the trim target values (Fig. 7(b)). All trim values are non-dimensionalized by W_0 (vehicle weight) and $W_0 R$. Both CA and CFD analysis results indicate that the desired convergence is achieved after about six coupling iteration steps, which ensures the validity and consistency of the CFD/CA LC approach employed in this study.

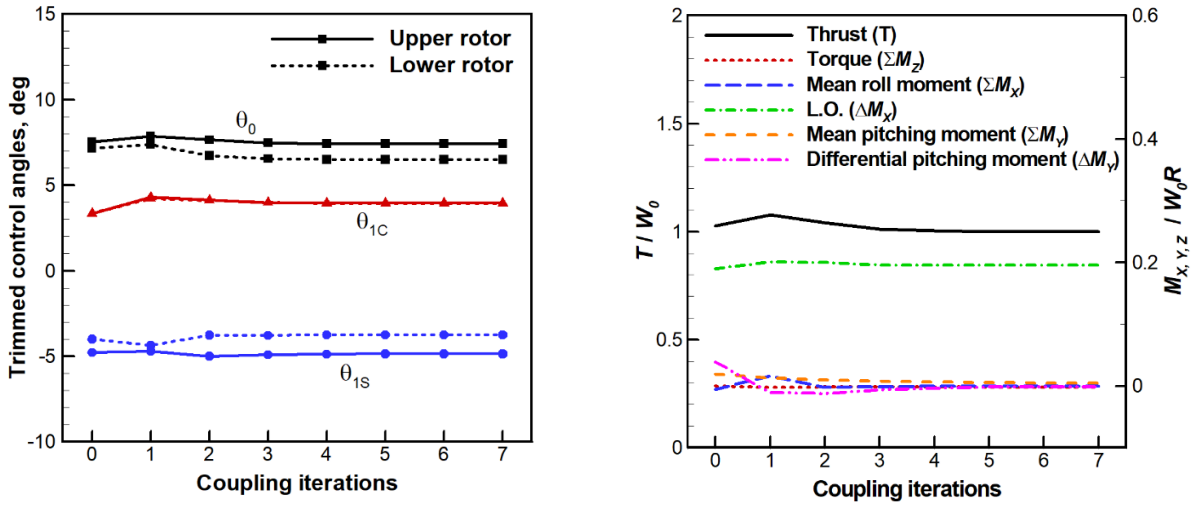

(a) Control trim angles (CA results) (b) Trim values (CFD results)

Fig. 7. CFD/CA convergence history for L.O. rotor in level flight (μ=0.397)

Validation of CFD/CA LC analysis

The predicted blade section normal and chord force coefficients are compared with the other CFD/CA analysis results[25]. It is noted that the same L.O. value of 0.2 adopted in former study[25] is used for fair comparison. Figure 8 shows the comparison of the sectional normal force and chord force coefficients obtained at the spanwise location of 0.75R in low-speed cruise (150 knots) condition. The present results indicate good agreements with the reference data, particularly in picking up the prominent peaks predicted around 240 and 300 azimuth angles. The peaks are due to the blade cross-over events of the counter-rotating rotors observed at the upper rotor[25]. The additional peculiar peak observed near 340 azimuth angle represents the self-induced root BVI events. All the blade cross-over events and BVI oscillation peaks are captured nicely by both CFD/CA LC methods. In contrast, CA predictions with the rolled-up free wake model (dotted lines) miss most of these unsteady events and predict nearly smoothened signal. Nevertheless, the CA results estimate the mean and the overall waveform of the airload profile reasonably well.

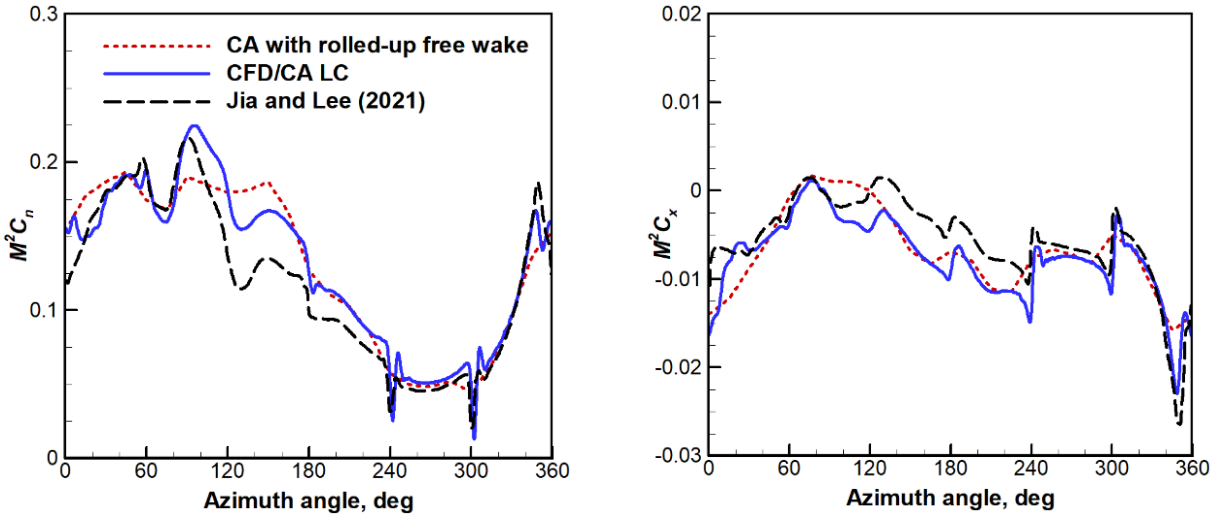

(a) Section normal force coefficient (M^2C_n) (a) Section chord force coefficient (M^2C_x)

Fig. 8. Comparison of section airloads at 0.75R in level flight (μ=0.397, upper rotor)

To further validate the present methodology of CFD/CA LC predictions, the L.O. coaxial rotorcraft at the speed of 200 knots is considered as well. Though not shown explicitly, the high-speed case (200 knots) showed a good convergence with respect to the coupling iterations. Figure 9 shows the comparison between the flight test data and the present results. Fig. 9(a) presents a comparison of the 3P (three per revolution) hub pitching moments (M_Y) evaluated between the CA with rolled-up free wake model and CFD/CA LC analysis in reference to the flight test data of XH-59A[4]. Since the actual L.O. value of the flight tests is unknown, the present results are computed using L.O. values of either 0.1 or 0.2, and they are presented together with the test data. The comparison results reveal that the CFD/CA LC with L.O. of 0.2 indicates a good correlation with the flight test data for 200 knot case. However, in case of 150 knots, L.O. value of 0.1 matches better with the test data. Some intermediate values between 0.1 and 0.2 may improve the correlation with the test data for 150 knots case. Fig. 9(b) shows a comparison of the effective lift-to-drag ratio (L/D_e) of the rotor with respect to the speeds. Both predictions obtained using the CA and CFD/CA LC show reasonable agreements with the flight test data over the speed range. In general, the isolated CA results with L.O. = 0.2 predict well, following the trend of the test data except at low speeds. The CFD/CA LC results with L.O. = 0.2 indicate improved correlations especially at the two specified flight speed speeds of either 150 or 200 knots. Overall, using the L.O. value of 0.2 appears to be a good estimate when examining the rotorcraft vibration for XH-59A at the speed of 200 knots. Figure 10 shows a Q-criterion contour plot colored by vorticity to illustrate the vortex trajectories of the two counter-rotating rotors in level forward speeds at 150 and 200 knots, respectively. The figures are plotted when the reference blades of both rotors are positioned at the rotor azimuthal angle of 300°, represents the instant when the blade cross-over occurs. It is observed that the formation of the vortex structures and their rolled-up processes are captured nicely for both flight conditions. As expected, the vortex structures dissipate more rapidly in 200 knots compared to the lower speed (150 knots) case.

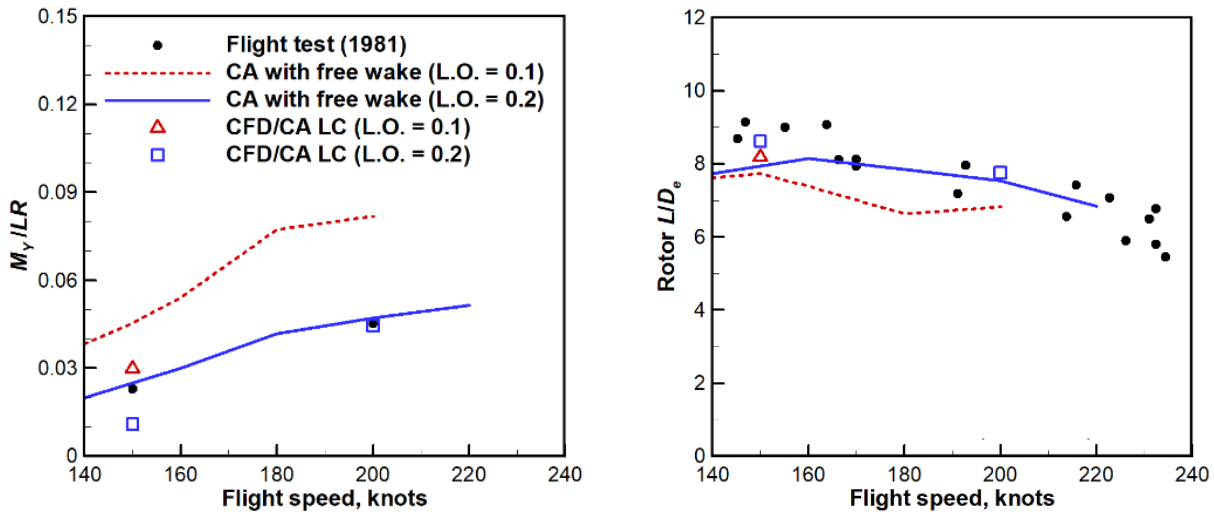

(a) 3P hub pitching moments (b) Rotor effective lift-to-drag ratios

Fig. 9. Comparison between flight test measurements and analysis results

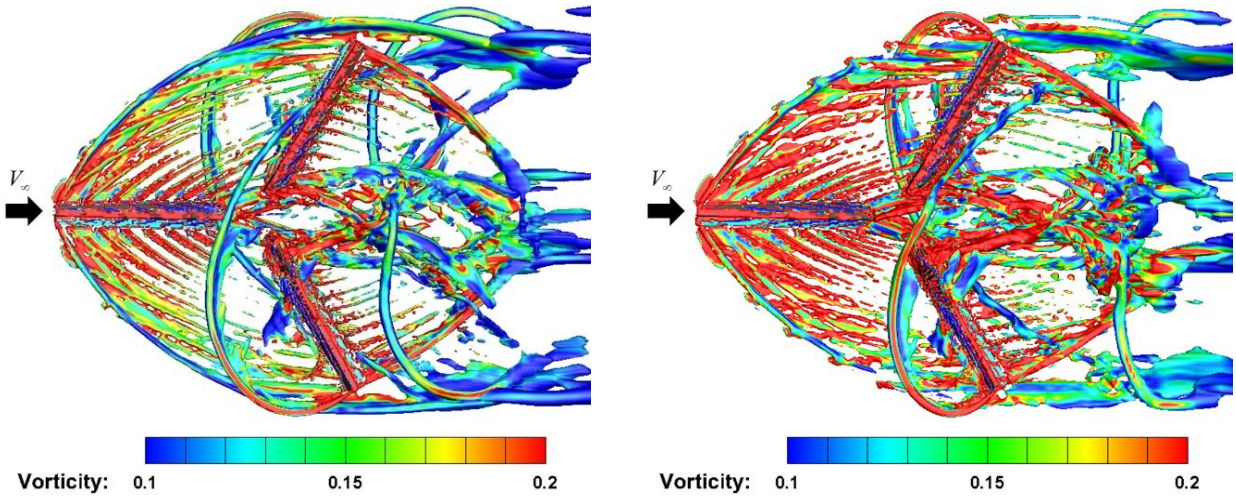

(a) 150 knots (μ=0.397) (a) 200 knots (μ=0.53)

Fig. 10. Q-criterion plot colored by vorticity for XH-59A in level forward flights (top view)

The above comparison reveals that the CFD/CA LC algorithm, trim strategy, and the detailed aeromechanics modeling are formulated and analyzed correctly in predicting the rotor hub vibrations for L.O. coaxial rotorcraft. The following sections investigate an active vibration reduction using the IBC actuation for the L.O. coaxial rotor in 200 knots. Retrimming is used when applying IBC actuations to maintain the same flight conditions as the baseline uncontrolled case.

Offline system responses to IBC

The offline system identification of the L.O. coaxial rotorcraft using the converged CFD/CA delta airloads is conducted next. The multicyclic vibration control is an effective technique that employs a linear, quasi-static, and frequency domain representation of a vehicle to minimize the vibration. In order to achieve a successful vibration control, it is desired to confirm the linearity of the system. This is confirmed by examining that the vibratory loads generated by independent control inputs are proportional to the actuation amplitudes, and their cosine and sine components are orthogonal with each other. Meeting the linearity criteria allows generating controllable vibratory loads with arbitrary amplitudes and phase angles[33]. Figure 11 shows 3P hub vibratory loads (F_X, F_Z, M_Y) responses due to IBC actuation inputs of single 3P or 4P harmonics while varying the amplitudes and phase angles. Note that the other loads components (F_Y, M_X, M_Z) are nor shown since they become canceled out by the nature of the counter-rotating rotor system. Only 3P and 4P actuation results are shown since 2P actuation indicates marginal vibration responses. It is observed that 4P IBC actuation profiles of M_Y indicate more sensitive to the vibratory responses than 3P actuation. It should be mentioned that the vibratory responses of the rotor represent a strong linear relationship between the actuation inputs and the resulting hub vibration responses. This clearly confirms that the current offline system satisfies the linearity, orthogonality, and quasi-static states of the multicyclic controls of the rotor.

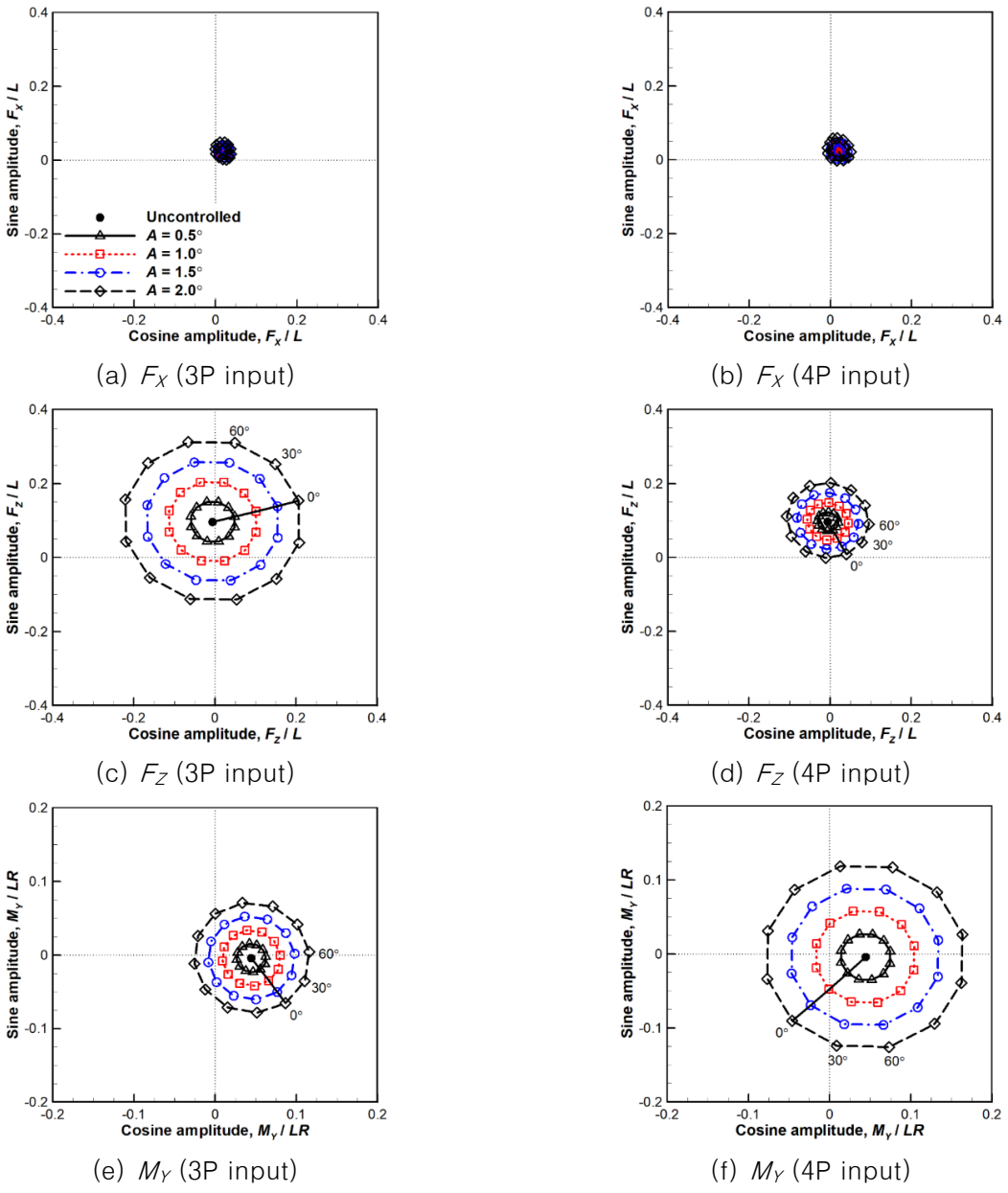

(a) F_X (3P input) (b) F_X (4P input)

(c) F_Z (3P input) (d) F_Z (4P input)

(e) M_Y (3P input) (f) M_Y (4P input)

Fig. 11. 3P vibratory responses of the rotor hub due to 3P or 4P IBC actuation inputs (amplitude and phase sweep)

The multicyclic controller using the identified offline system is validated next, in reference to the parametric sweep study results. To this end, the optimal control results are computed using a multicyclic controller with each harmonic set as the only control variable. The optimum controller is adjusted using the weight matrix W_θ which is given by:

$$W_\theta = d \times I_\theta \tag{17}$$

where d is an arbitrary number and I_θ is the identity matrix corresponding to the size of θ, respectively. The IBC actuation authority is limited to 2.0 deg., as in the case of the parametric sweep study, for a consistency. The weight matrix of the vibration response W_z is then defined as:

$$W_z = \mathrm{diag}(0.5, 0, 1, 0, 1, 0, 0.5, 0, 1, 0, 1, 0) \tag{18}$$

where the respective weight factors correspond to the respective cosine and sine components of the vibratory hub loads chosen according to the weights of the vibration indices defined in Eq. (2). The zero entities reflect the negligible vibratory loads components (F_Y, M_X, M_Z), considering the cancellation effects by the counter-rotating rotors. Figure 12 shows the rotor hub vibration levels (VI), computed using the open-loop multicyclic controller with offline system identification (Fig. 5) and the parametric sweep study results, respectively. The results indicate that the optimal solutions are predicted the best vibration reduction correctly for each case of the harmonic actuations, as the actuation frequency is varied from 2P to 4P. The simulation results also show a close correlation between the optimal solutions and the parametric sweep study results.

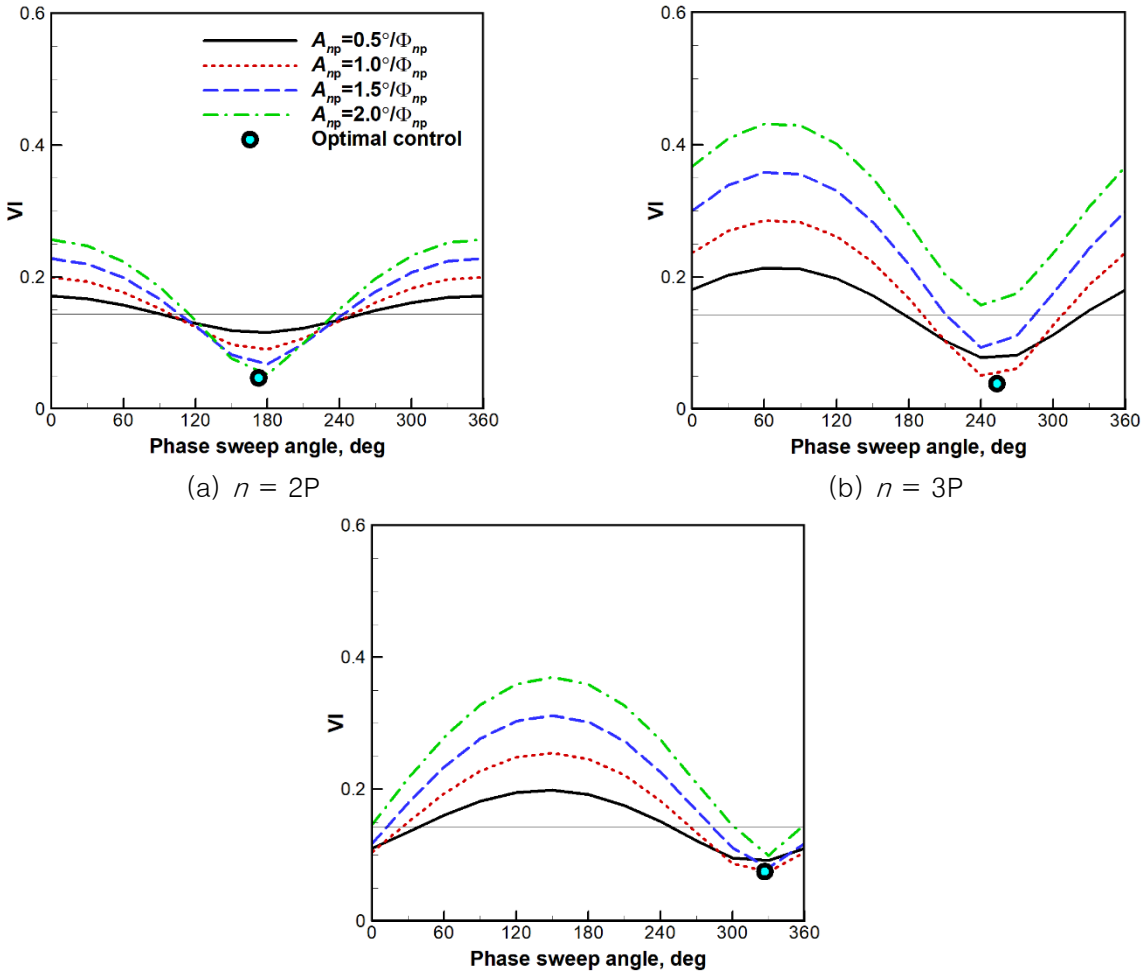

(a) n = 2P

(b) n = 3P

(c) n = 4P

Fig. 12. Comparison of 3P rotor hub vibration VI

In summary, the behavior of the vibratory responses due to the IBC actuation inputs demonstrated an apparent linearity and excellent agreements with the parametric sweep study results, ensuring the validity of the offline identification system and the multicyclic controller, respectively. In the following section, the optimal frequency contents of the multicyclic control are investigated while exploiting an open-loop control performed based on the CFD/CA delta airloads, with the goal of reducing the rotor hub vibration.

Open-loop control

An open-loop multicyclic control is performed to examine the influence of single and multiple harmonic actuations on vibration responses of the L.O. coaxial rotor. The analysis adopts the converged CFD/CA delta airloads to determine the optimal frequency contents of the subsequent closed-loop control approach within the CFD/CA LC framework (Fig. 6). The actuation pitch amplitudes θ_{nc} of the multicyclic controller is limited to ±3 deg. considering the wind tunnel test results of IBC actuation conducted for UH-60A[34].

Figure 13 compares the rotor hub vibration index VI predicted using CA analysis with either a rolled-up free wake model or CFD/CA converged delta airloads when applying different IBC harmonic inputs. The baseline hub vibration results with no control obtained using the CFD/CA LC analysis are included as a reference. Each data point in Fig. 13 represents the minimum vibration condition achieved at each active harmonic input. The simulation results on rotor hub VI demonstrate that an IBC actuation with specific harmonics (single or multiple) is effective in reducing the hub vibration. Notably, optimal control performances vary substantially depending on the actuation scenarios with different harmonics. For the rolled-up free wake model, the best performance is reached at 2P single input, whereas the delta airloads approach shows the best reduction gain with 3P input. When multiple harmonics is applied, more vibration reduction gains are obtained than the single harmonic cases. Specifically, the (3P+4P) combination provides the greatest vibration suppression with the rolled-up free wake model, whereas the (2P+3P+4P) input results in the best reduction with the delta airloads approach. The resulting vibration reduction reaches approximately 83.7% and 89.1% for the respective multi-harmonic actuation cases. Compared to the best single-harmonic application, the multiple harmonic input (2P+3P+4P) shows an additional 16% reduction in rotor hub vibration, highlighting the superiority of the multi-harmonic IBC control, as compared with the single harmonic case.

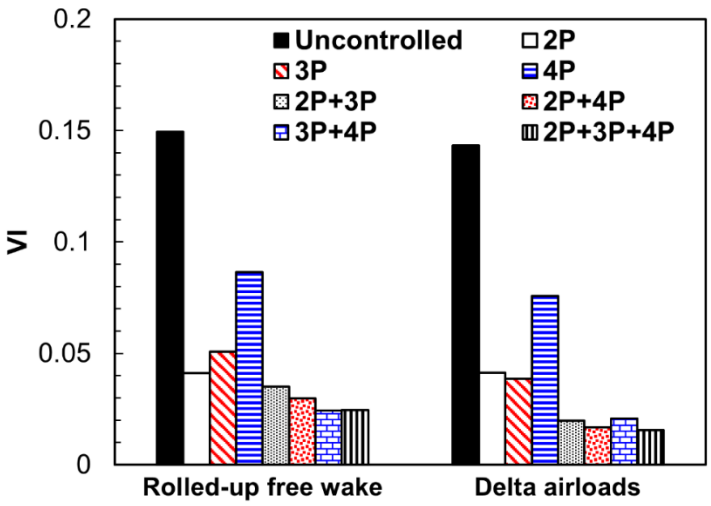

Fig. 13. Effect of delta airloads on open-loop control

To assess the accuracy of the identified frequency contents in the multicyclic control, a closed-loop control using a 3P IBC actuation is performed next using CFD/CA LC analysis.

Closed-loop single harmonic control

The closed-loop multicyclic control offers the benefit of incorporating the step-size α to regulate the system response. Appropriate selection of α ensures the smooth transition of control inputs, preventing abrupt changes in control system responses. This results in achieving a minimum vibration state without

overburdening the actuators. The closed-loop multicyclic controller is explored using the 3P IBC input for the best vibration reduction case. It should be noted that the closed-loop control using CFD/CA LC is conducted to evaluate the accuracy of the vibration reduction gains as well as the validity of the optimal control solutions. The same system model $\hat{T}$ and the weight matrices W_Z, W_θ, and $W_{\Delta\theta}$ adopted in the open-loop control study are employed. A gradient descent algorithm is used to perform the closed-loop control simulation. An appropriate selection of the step-size α will be crucial in the gradient descent search.

Figure 14 shows the effect of α on the convergence behavior of 3P hub vibration using the closed-loop control, as α varies from 10 to 150. It is observed that the convergence becomes improved, as α increases up to about 80. Around the time step-size of 80, the system appears to converge to the optimal control solution. However, as α increases further, the system is no more converged to the optimal solution and the system response oscillates or diverges. Based on the convergence results, α is selected as 70 for the closed-loop control study. Figure 15 shows the first 8 iterations of the closed-loop control responses for the 3P harmonic actuation on the rotor hub vibration. Both predictions obtained using CA with rolled-up free wake and CFD/CA LC analyses are compared in the plot. The results indicate rapid convergence, with more vibration reduction gains by CFD/CA LC approach. In Figure 16, the hub vibratory loads results (F_X, F_Z, M_Y) using the two different methods are presented. The other hub load components (F_Y, M_X, M_Z) are not shown because of the cancellation effects as mentioned earlier. The baseline uncontrolled results are obtained using CFD/CA LC analysis. It is observed that there is a significant difference between the two closed-loop control results in predicting the minimum hub vibrations of the rotor. As compared to the CFD/CA LC, the CA model method overpredicts VI by 10.8% and underpredicts F_X by 55.7%. The vibration reduction by optimal controls of CFD/CA LC analysis is approximately 13% for longitudinal hub force F_X, 92.0% for vertical hub force F_Z, and 55.4% for pitching hub moment M_Y respectively, resulting in 73.4% in the overall rotor hub vibration. These results demonstrate the necessity of using high-fidelity CFD/CA LC analysis for more precise estimation of the optimal vibration reduction. It should be mentioned that this outcome comes with heavier computational costs for CFD/CA LC analysis in which a total of 35.5 hours are consumed using an Intel Xeon Gold 6430 PC with 112 cores (approximately 237 minutes per iteration). In contrast, only about 2.7 hours are needed for CA with free wake model using a single core.

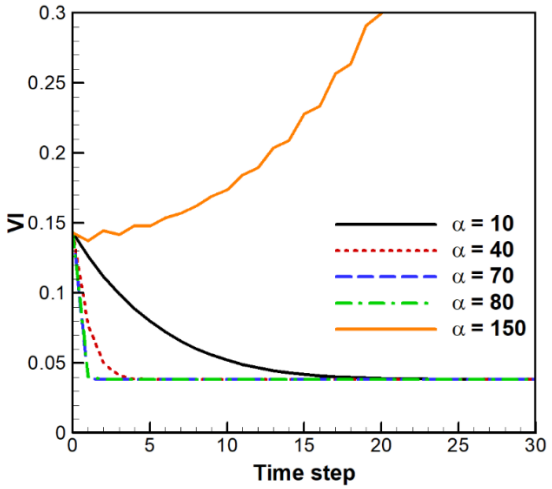

Fig. 14. Effect of the step size α in closed-loop controller using 3P IBC actuation

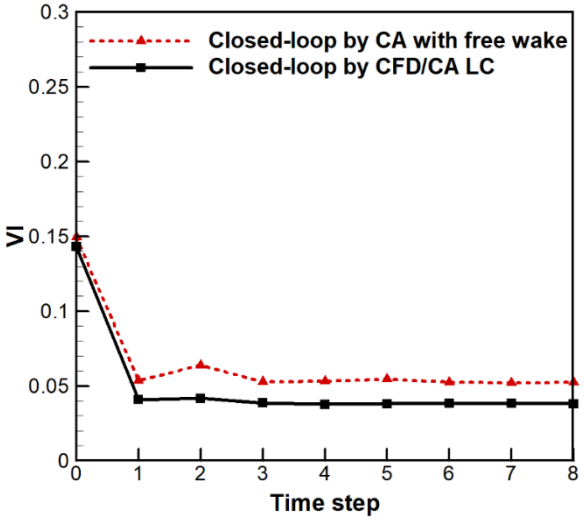

Fig. 15. Comparison of rotor vibration responses

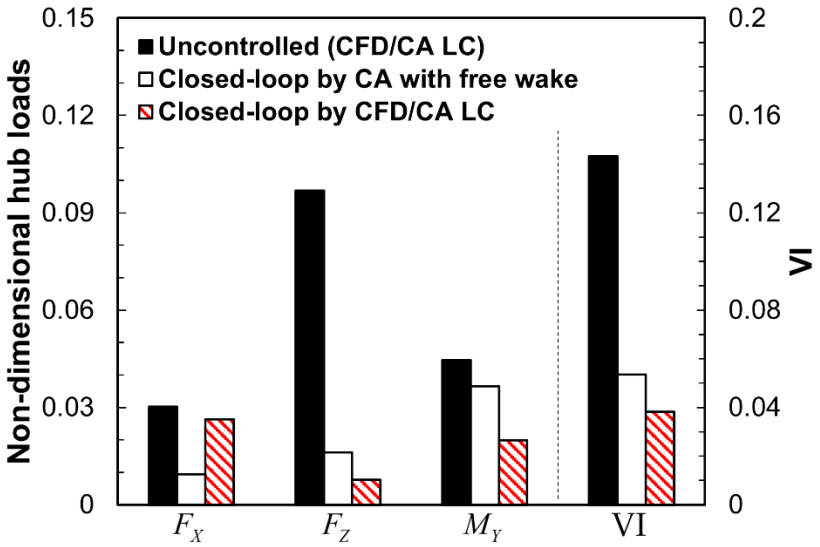

Fig. 16. Comparison of vibratory responses using 3P optimal controls

In Figure 17, the converged closed-loop optimal control results with 3P IBC actuation are compared between the CA-alone and CFD/CA LC approaches. It is shown that there exist substantial deviations in predicting the amplitudes and phases of the minimum vibration: the CA with rolled-up free wake model overestimates the IBC amplitudes by up to 30.9% with a phase offset of about 10.9 deg. The discrepancies indicate the importance of implementing the high-fidelity CFD/CA LC analysis to generate the correct actuation profiles. To confirm whether the closed-loop control via CFD/CA LC yields the true optimal control solution, a parametric sweep study is conducted. Figure 18 compares the parametric sweep study results obtained using either CA (dashed lines) or CFD/CA LC (solid lines) analysis when 3P single harmonic inputs are applied to the rotor. The closed-loop optimal solution is also incorporated (as solid circles) for the comparison. The closed-loop optimal control solution indicates a 3P harmonic actuation with the phase angle of 246.5 degree (Fig. 18(a)) and amplitude of 0.81 degree (Fig. 18(b)). Considering the heavy computational costs of CFD/CA LC analyses, only the nearby phase angles or the amplitude cases are varied, in reference to the optimal control solutions. Inspecting the results reveals that the present closed-loop control methods yield the optimal control solutions precisely, thereby confirming the adequacy of the present control methodology. It is indicated that the CA

predictions with rolled-up free wake model substantially underestimate the vibration reduction gains by maximum about 25.4%. Furthermore, both the amplitudes and phases of 3P IBC actuation with the CA analysis indicate apparent offsets with the closed-loop optimal solution with CFD/CA LC analysis. This observation assures the reliability and high precision of the present closed-loop control schemes of the optimum vibration reduction for L.O. coaxial rotor. In the following section, the closed-loop control is extended to cover the multicyclic control strategy.

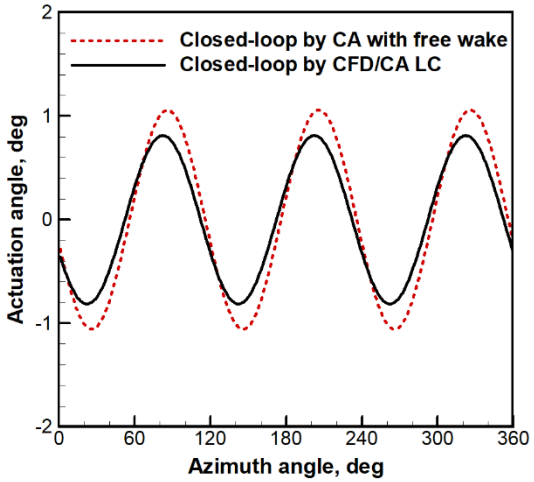

Fig. 17. Comparison of control actuations between rolled-up free wake and CFD/CA LC analysis

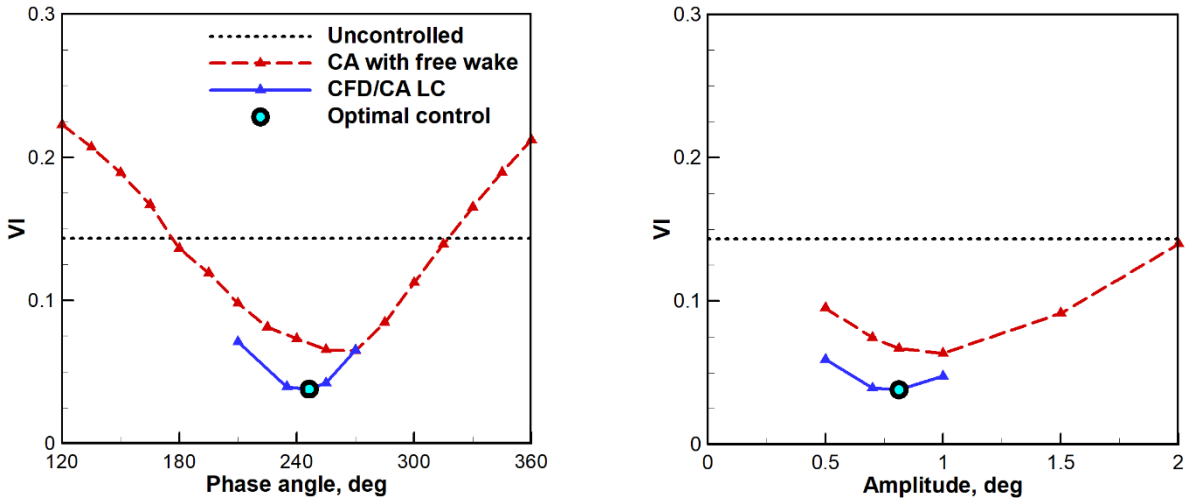

(a) Changes in phase angles with the amplitude fixed at 0.812 deg.

(b) Changes in amplitudes with the phase angle fixed at 246.5 deg.

Fig. 18. Comparison of parametric sweep results (CA vs. CFD/CA LC) with respect to 3P optimal closed-loop control solutions

Closed-loop multicyclic control

Two different multicyclic controls using (2P+4P) and (2P+3P+4P) IBC actuations are implemented next to evaluate the effectiveness in reducing the rotor hub vibration. These combined frequency inputs identified previously as the optimal open-loop control inputs (Fig. 13) are adopted in the closed-loop study. The step-sizes α for each case are determined according to the sensitivity analyses. Figure 19 shows the influence of varying α on the convergence behavior of the respective closed-loop controllers.

The step-sizes are determined as 150 for (2P+4P) and 50 for (2P+3P+4P) actuations, respectively. Figure 20 presents the resulting hub vibration responses for both multicyclic actuation cases. In both cases, about 20 time steps are seen to be required to reach a convergence. The results indicate that either one of actuation strategies yield significant vibration reductions, with the final converged results being nearly identical. The results confirm also the effectiveness of the present closed-loop multicyclic controls in suppressing the rotor hub vibration of the L.O. coaxial rotor.

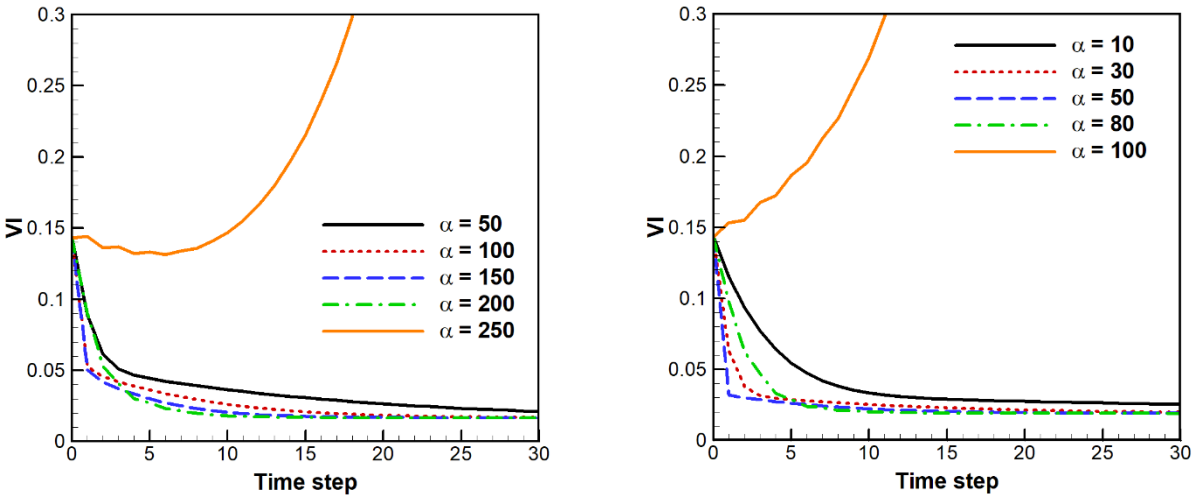

(a) (2P+4P) actuation (b) (2P+3P+4P) actuation

Fig. 19. Effect of α on closed-loop controller for multicyclic IBC actuation

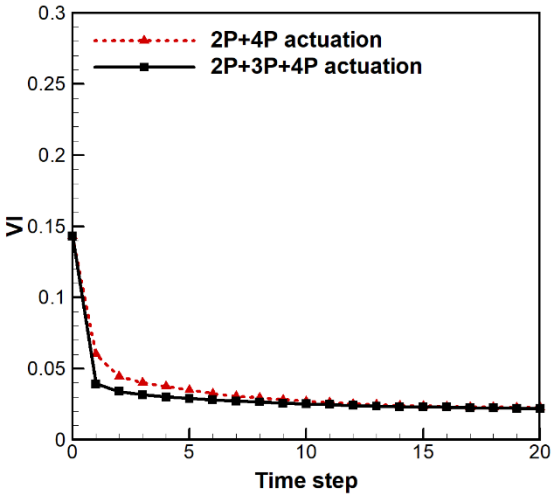

Fig. 20. Comparison of rotor hub vibration responses

Figure 21 presents the optimal vibration reduction results obtained for specified multicyclic IBC inputs applied through the closed-loop control of the CFD/CA LC approach. The cases of either the uncontrolled or 3P single harmonic actuation are included for reference purpose. It is seen that the reductions in longitudinal hub force F_X remain relatively modest, reaching a maximum of 21.6% with the (2P+3P+4P) actuation. In contrast, the vertical hub force F_Z and pitching moment M_Y exhibit large reductions. Specifically, the (2P+4P) actuation achieves vibratory loads reductions of 97.3% and 94.3% for F_Z and M_Y, respectively, as compared with the uncontrolled case. The (2P+3P+4P) actuation shows comparable performance, with reductions by 97.1% and 91.5% for F_Z and M_Y components,

respectively. Overall, it leads to a maximum hub vibration reduction by 84.7% when the multicyclic (2P+3P+4P) input is applied.

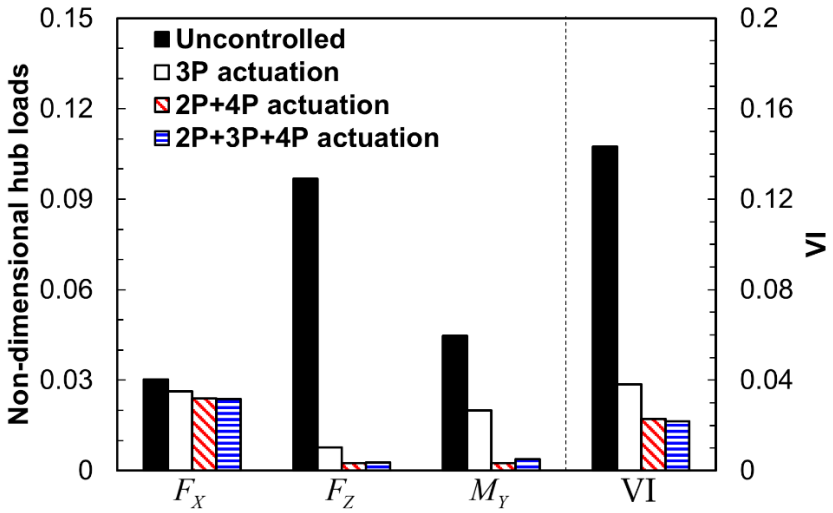

Fig. 21. Comparison of vibratory responses using the optimal reduction scenarios

Figure 22 shows the optimal IBC actuation profiles (Fig. 22(a)) and the total blade geometric pitch angles (Fig. 22(b)) over the rotor revolution, predicted respectively using the single 3P and the multiple (2P+4P) or (2P+3P+4P) actuations. Generally, the waveforms of the different harmonic pitch inputs indicate a consistent down-up pattern in the first quadrant of the rotor disk (Fig. 22(a)). The second quadrant signals also exhibit close similarity, especially between the 3P and (2P+3P+4P) control scenarios, with significantly reduced pitch amplitudes compared to (2P+4P) actuation. As expected, the retreating side signals display rather arbitrary profiles between the actuation cases, primarily due to the nature of the L.O. coaxial rotor system, where the retreating region is off-loaded with playing less roles in generating the rotor lift. Fig. 22(b) illustrates the blade total geometric pitch angle variations between the different IBC inputs. Retrimming is used for each actuation case. Other than the primary pitch control, the additional higher harmonics due to IBC inputs is evident, influencing the trimmed control angles over the rotor disk.

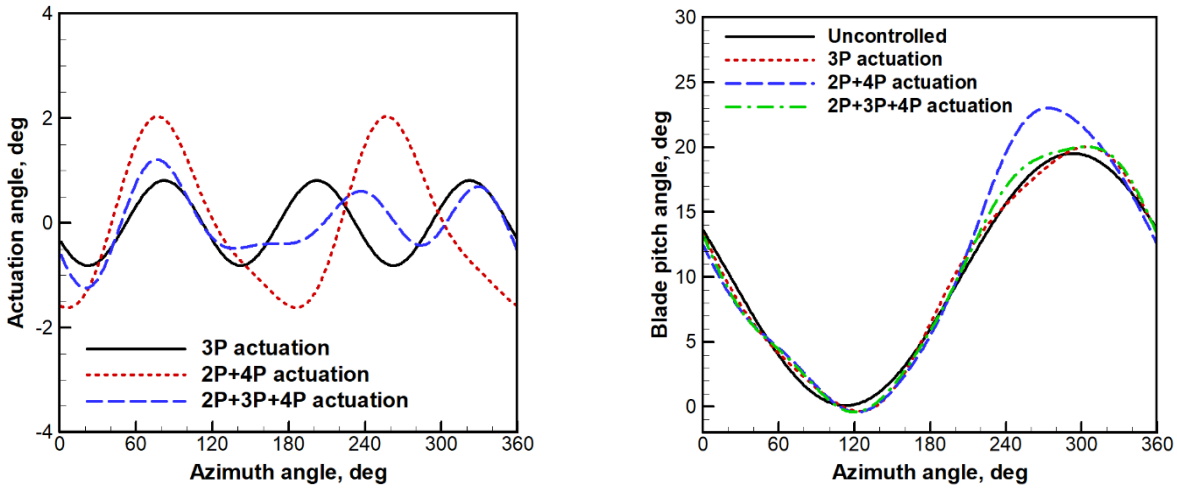

(a) IBC actuation angle (b) Blade geometry pitch angle (r/R=0.75)

Fig. 22. Comparison of the optimal actuation scenarios

The changes in airloads distributions before and after the IBC actuations and their mechanism leading to a reduction in the rotor hub vibration are investigated next. Figure 23 compares the sectional normal force distributions of both rotors in contour format between the baseline uncontrolled and the optimal (2P+3P+4P) actuation cases. As can be seen, the sectional airloads over the rotor disk become altered and redistributed, particularly in the advancing side, due to the application of the IBC actuation pitch inputs. In the lower rotor, the high loading zones (red color) positioned near 30° or 150° shift to around 90° as the actuation input (2P+3P+4P) (Fig. 23(b)). This observation can also be found in the upper rotor where the high loading zones positioned near 30° or 150° shift to around 90°. In addition, the strong negative tip loading zones in the first quadrant (Fig. 23(a)) become shift to the second quadrant with the application of the active inputs (Fig. 23(b)). Overall, the redistributions of airloads with substantially decreased peaks in the section normal force signals contribute to reducing the hub vibration levels of the L.O. coaxial rotor in high-speed flight.

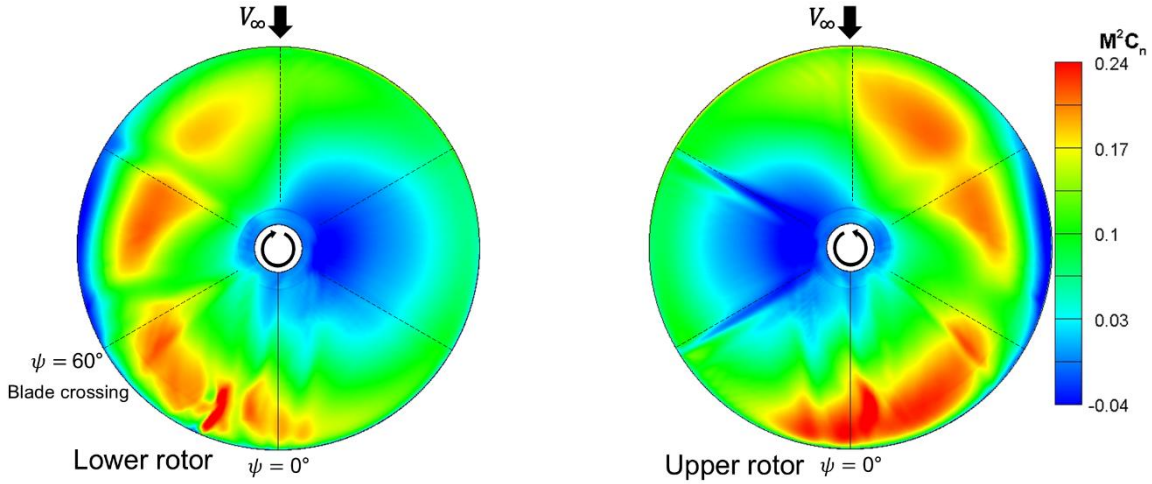

(a) Baseline (uncontrolled)

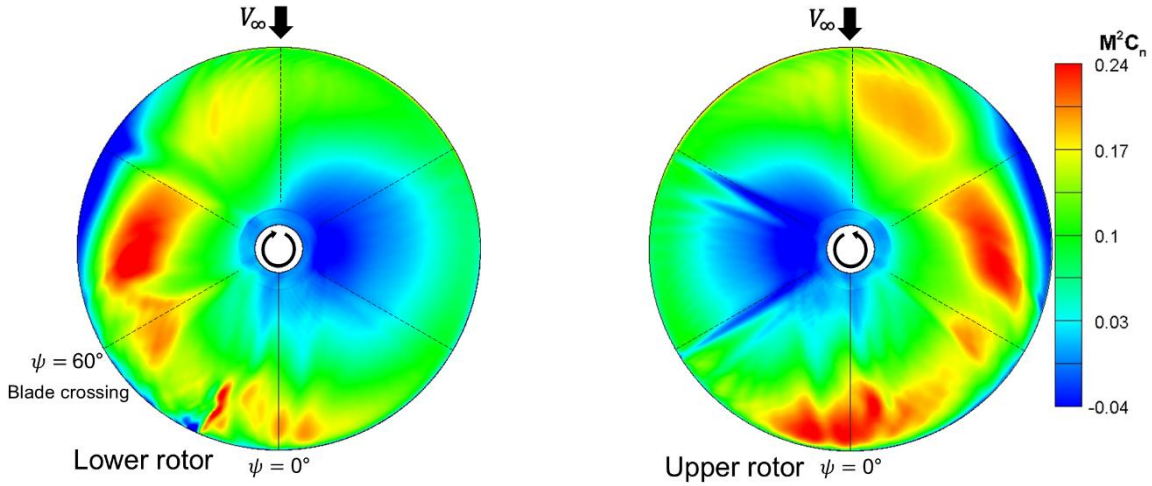

(b) Optimal control (2P+3P+4P)

Fig. 23. Contour plots comparing sectional normal force distributions over the rotor disk

Conclusions

In this study, an active vibration reduction of XH-59A rotor in high-speed forward flight was investigated using multicyclic control strategies combined with CFD/CA LC framework. A 3D compressible RANS flow solver KFLOW and rotorcraft CA code CAMRAD II were loosely coupled to carry out the LC analysis. Both the open- and closed-loop control schemes were adopted to determine the minimum vibrations of the rotor. The following conclusions were drawn from the present investigation:

1) The CFD/CA LC analysis resulted in a good convergence in reaching the trim of the L.O. coaxial rotor. Both the predicted hub vibration and rotor lift-to-drag ratio were correlated with the flight test data, demonstrating the validity and accuracy of the LC algorithm.

2) The open-loop control simulations led to identifying dominant actuation frequencies in reducing the rotor hub vibrations: (3P+4P) for CA with rolled-up free wake model and (2P+3P+4P) for CFD/CA LC approach, respectively.

3) The closed-loop control with CFD/CA LC approach was performed using a single 3P harmonic input, achieving significant hub vibration reductions up to 73.4% as compared with the uncontrolled case. The parametric sweep study results assured the optimal IBC actuation condition clearly, with correct prediction on the amplitude and phase responses.

4) Comparing with the closed-loop control results using the CFD/CA LC approach revealed that the CA with rolled-up free wake model substantially underestimated the hub vibration reduction by 25.4%, with apparent offsets in predicting the amplitudes and phases of the minimum vibration condition.

5) The multicyclic controller using a (2P+3P+4P) IBC input resulted in 3P hub vibration reduction of about 84.7%, with significant decreases in the vibratory hub loads components. Investigating the rotor flow field revealed that the pitch angles became adjusted to redistribute the sectional airloads, alleviate the peak loadings, and shift the negative tip loading zones from the first quadrant to the second quadrant, overall leading to significantly reduced vibrations.

References

[1] D. Walsh, S. Weiner, K. Arifian, T. Lawrence, M. Wilson, T. Millott, “High Airspeed Testing of the X2 Technology™ Demonstrator,” American Helicopter Society 67th Annual Forum Proceedings, Virginia Beach, VA, May 4, 2011.

[2] C. Öhrle, F. Frey, J. Thiemeier, M. Keßler, E. Krämer, M. Embacher, P. Cranga, P. Eglin, “Compound Helicopter X^3 in High-Speed Flight: Correlation of Simulation and Flight Test,” Vertical Flight Society 75th Annual Forum Proceedings, Philadelphia, PA, May 13-16, 2019.

[3] J. Zhao, M. Wilson, W. Welsh, “S-97 Raider® Maneuvering Loads Flight Test and Simulation Correlation,” Vertical Flight Society 79th Annual Forum Proceedings, West Palm Beach, FL, May 16-18, 2023.

[4] A. J. Ruddell, W. Growth, R. McCutcheon, “Advancing Blade Concept (ABC) Technology Demonstrator,” US Army Research and Technology Laboratories, USAAVRADCOM-TR-81-D-5, Apr. 1981.

[5] A. J. Ruddell, “Advancing Blade Concept (ABC™) Development,” Journal of the American Helicopter Society, Vol. 22, No. 1, pp. 13-23, Jan. 1977.

[6] J. C. Ho, H. S. Yeo, "Analytical Study of an Isolated Coaxial Rotor System with Lift Offset", Aerospace Science and Technology, Vol. 100, 2020, Paper No. 105818.

[7] C. G. Cameron, J. Sirohi, J. Schmaus, I. Chopra, “Performance and Loads of a Reduced-Scale Coaxial Counterrotating Rotor,” Journal of the American Helicopter Society, Vol. 64, No. 4, Oct. 2019.

[8] R. Blackwell, T. Millott, “Dynamic Design Characteristics of the Sikorsky X2 Technology Demonstrator Aircraft,” American Helicopter Society 64th Annual Forum Proceedings, Montreal, Canada, Apr. 29-May 1, 2008.

[9] Y.-L. Lee, D.-H. Kim, J.-S. Park, S. B. Hong, “Vibration Reduction Simulations of a Lift-Offset Compound Helicopter Using Two Active Control Techniques,” Aerospace Science and Technology, Vol. 106, 2020, Paper No: 106181.

[10] S. H. Hong, D. K. Kim, S. N. Jung, “Individual Blade Control Approach for Active Vibration Suppression of a Lift-Offset Coaxial Rotorcraft,”, Journal of Aircraft, Apr. 2024.

[11] I. Mawry, E. Smith, S. Schmitz, J. Zhang, J. S. Park, "Fuselage Vibration Reduction of Lift-Offset Coaxial Rotor Vehicles with Auxiliary Propulsion via Individual Blade Pitch Control (IBC)," 50th European Rotorcraft Forum Proceedings, Marseille, France, Sep. 10-12, 2024.

[12] S. H. Hong, S. N. Jung, D.-H. Kim, "Active Vibration Suppression of Lift-Offset Coaxial Rotorcraft Using Multicyclic Control," AIAA Journal, Dec. 2024.

[13] K. Hayami, H. Sugawara, T. Yumino, Y. Tanabe, M. Kameda, “CFD-based performance analysis of a coaxial rotor with lift-offset in high advance ratio flight,” Aerospace Science and Technology, Vol. 135, 2023, Paper No: 107272.

[14] X. Yuan, W. Bian, Q. Zhao, G. Zhao, “Numerical investigation of aerodynamic interactions for the coaxial rotor system in low-speed forward flight,” Aerospace Science and Technology, Vol. 149, 2024, Paper No: 109184.

[15] C. Tung, F. X. Caradonna, W. Johnson, “The prediction of transonic flows on an advancing rotor,” Journal of American Helicopter Society, Vol. 31, pp. 4-9. 1986.

[16] W. G. Bousman, “Putting the aero back into aeroelasticity,” In Proceedings of the Eighty ARO Workshop on Aeroelasticity of Rotorcraft Systems, State College, PA, USA, Oct. 1999, pp. 18-20.

[17] R. Kufeld, W. G. Bousman, “UH-60A helicopter rotor airloads measured in flight,” Aeronautical Journal, Vol. 101, pp. 217-227, 1997.

[18] M. Potsdam, H. Yeo, W. Johnson, “Rotor airloads prediction using loose aerodynamic/structural coupling,” Journal of Aircraft, Vol. 43, pp. 732-742, 2006.

[19] A. Datta, J. Sitaraman, I. Chopra, J. D. Baeder, “CFD/CSD prediction of rotor vibratory loads in

high-speed flight," Journal of Aircraft, Vol. 43, pp. 1698-1709, 2006.

[20] B. Ortun, M. Potsdam, H. Yeo, K. V. Truong, "Rotor loads prediction on the ONERA 7A rotor using loose fluid/structure coupling," American Helicopter Society 72nd Annual Forum Proceedings, West Palm Beach, FL, USA, May 17-19, 2016.

[21] F. Richez, "Analysis of dynamic stall mechanisms in helicopter rotor environment," Journal of American Helicopter Society, Vol. 63, pp. 1-11, 2018.

[22] Y. H. You, D. H. Na, S. N. Jung"Improved rotor aeromechanics predictions using a fluid structure interaction approach," Aerospace Science and Technology, Vol. 73, pp. 118-128, 2018.

[23] M. J. Smith, J. W. Lim, B. G. van der Wall, J. D. Baeder, R. T. Biedron, D. D. Boyd Jr., B. Jayaraman, S. N. Jung, B. Y. Min, "The HART II international workshop: An assessment of the state of the art in CFD/CSD Prediction," CEAS Aeronautical Journal, Vol. 4, pp. 345-372, 2013.

[24] S. N. Jung, J. H. Sa, Y. H. You, J. S. Park, S. H. Park, "Loose Fluid-Structure Coupled Approach for a Rotor in Descent Incorporating Fuselage Effects," Journal of Aircraft, Vol. 50, No. 4, pp. 1016-1026, Jul. 2013.

[25] Z. Jia, S. Lee, "Aerodynamically induced noise of a lift-offset coaxial rotor with pitch attitude in high-speed forward flight," Journal of Sound and Vibration, Vol. 491, 2021, Paper No. 115737

[26] B.-Y. Min, J. Kim, V. Klimchenko, J. C. Neiswonger, D. Griffiths, B. E. Wake, "Full vehicle Helios model performance correlation with SB>1 Defiant flight test," Vertical Flight Society 80th Annual Forum Proceedings, Montreal, Canada, May 7-9, 2024.

[27] W. Johnson, "CAMRAD II: Comprehensive Analytical Model of Rotorcraft Aerodynamics and Dynamics," Johnson Aeronautics, Palo Alto, CA, 1992.

[28] J. W. Kim, S. H. Park, Y. H. Yu, "Euler and Navier-Stokes simulations of helicopter rotor blade in forward flight using an overlapped grid solver," AIAA Paper 2009-4268, 19th AIAA CFD Conference, 2009.

[29] S. N. Jung, Y. H. You, J. W. Kim, J. H. Sa, J. S. Park, S. H. Park, "Correlation of aeroelastic responses and structural loads for a rotor in descending flight," Journal of Aircraft, Vol. 49, pp. 398-406, 2012.

[30] W. Johnson, "A general free wake geometry calculation for wings and rotors," American Helicopter Society 51st Annual Forum Proceedings, Forth Worth, TX, May 9-11, 1995.

[31] Anonymous, "Aeronautical Design Standard Practice: Requirements for Rotorcraft Vibration Specifications, Modeling, and Testing," ADS-27A-SP, US Army Aviation and Missile Command, Redstone Arsenal, AL, 2006.

[32] W. Johnson, "Self-tuning regulators for multicyclic control of helicopter vibration," NASA-TP-1996, Mar. 1982.

[33] D.-H. Kim, S. H. Hong, S. N. Jung, "Multicyclic vibration control of a helicopter rotor with active twist actuation," International Journal of Aeronautical and Space Sciences, Vol. 23, pp. 303-314, 2022.

[34] T. R. Norman, C. Theodore, P. Shinoda, D. Fuerst, U. T. Arnold, S. Makinen, P. Lorber, J. O'Neill, "Full-scale Wind Tunnel Test of a UH-60 Individual Blade Control System for Performance Improvement and Vibration, Loads, and Noise Control," American Helicopter Society 65th Annual Forum Proceedings, Grapevine, TX, May 2009.